Short Note

Equivalence of source-receiver migration and shot-profile migration

Biondo Biondi

Stanford Exploration Project, Mitchell Bldg., Department of Geophysics,

Stanford University, Stanford, CA 94305-2215

(March 1, 2005)

INTRODUCTION

At first glance, shot-profile migration (Jacobs, 1982) and source-receiver (survey-sinking) migration (Claerbout, 1985) seem to be substantially different algorithms. The basic principles used by the two schemes are different. Shot-profile migration is performed by *independently* propagating the source wavefield and the receiver wavefield. The image is obtained by cross-correlating the two wavefields (possibly normalized by the amplitude of the source wavefield). Source-receiver migration is based on the concept of survey sinking, by which we recursively synthesize equivalent data sets at increasing depth. At each depth step, imaging is performed by extracting the wavefield at zero time.

Recently the issue of the relation between shot-profile migration and source-receiver migration has become more relevant because of two important developments: 1) the increase in the practical applications of 3-D prestack migration by wavefield continuation for imaging complex structures, 2) the introduction of methods for computing Angle-Domain Common Image Gathers (ADCIG), both for velocity estimation (Prucha et al., 1999; Biondi and Sava, 1999; Clapp and Biondi, 2000) and for Amplitude Versus Angle (AVA) analysis (de Bruin et al., 1990; Wapenaar et al., 1999; Sava et al.,

2001).

Depending on the acquisition geometry, the efficiency of 3-D shot-profile migration can be substantially different from the efficiency of 3-D source-receiver migration. In general, source-receiver migration is more attractive for marine data that have limited azimuthal range (Biondi and Palacharla, 1996), while shot-profile migration is better suited for land or Ocean Bottom Cable (OBC) acquisition geometries. Jeannot (1988) discussed some practical aspects and the relative advantages of source-receiver and shot-profile migration for 2-D data. Most of his observations are also valid for 3-D data. When choosing between these two migration methods, it is important to realize that in principle the two methods are equivalent.

The application to velocity estimation of the ADCIGs obtained by source-receiver migration was first proposed by Biondi and Sava (1999) and Sava et al. (2001). Rickett and Sava (2002) extended one of these methods for computing ADCIGs by source-receiver migration (Sava et al., 2001) to the computation of ADCIGs by downward-continuation shot-profile migration. Biondi and Shan (2002) further extended the work of Rickett and Sava (2002) to reverse-time shot-profile migration. These two extensions depend on the "equivalence" of the offset-domain CIGs computed by shot-profile migration and source-receiver migration.

In this short note I demonstrate theoretically that the two migration methods produce exactly the same image and provide the same velocity and AVA information. This important result is based on the demonstration that the two methods produce the same image cube; that is, the images are the same not only at zero subsurface offset (migrated image), but also at non-zero subsurface offset (velocity and AVA information). This result implies that both the quality of the migrated image and the accuracy of the velocity updating information are independent from the choice between source-receiver migration or shot-profile migration. I illustrate the theoretical result by comparing the migrated im-

ages, including the offset-domain CIGs and the ADCIGs, for a synthetic data set with strong lateral velocity variations.

Berkhout (1984) and Wapenaar and Berkhout (1987) already addressed the issue of the theoretical equivalence between source-receiver migration and shot-profile migration. This short note goes beyond their theoretical result because it discusses, and illustrates with an example, the implications of the theory for the computation of ADCIGs. Therefore, I extend the relevance of the theoretical result to both velocity estimation and AVA analysis by wavefield continuation methods. Furthermore, I validate the theoretical result with a numerical example.

I demonstrate the identity of the two methods when shot-profile migration satisfies three specific requirements: 1) the source function is an impulse at zero time and a delta function in space, 2) the imaging condition is the cross-correlation of the source wavefield by the receiver wavefield, and 3) the source and receiver wavefields are propagated by downward continuation (i.e. not by reverse-time propagation). Another obvious assumption is that the same numerical algorithm is employed to downward continue the wavefields for both migration methods. Requirement 1) could actually be lifted (Wapenaar and Berkhout, 1987), but at the expense of additional complexity in the theory, which might obfuscate the fundamental concepts.

The equivalence of the two migration methods is based on the linearity of migration and on the commutative properties of the downward-continuation operator that I demonstrate in Appendix A. The demonstration of the equivalence becomes fairly simple when we consider the migration of a single shot record by source-receiver downward continuation. In this case, the downward continuation of the sources performed during source-receiver migration is equivalent to the multiplication of the downward-continued receiver wavefield with shifted copies of the complex-conjugated (time-reversed) source wavefield generated by an impulsive source. This multiplication is equivalent to

the cross-correlation of the receiver wavefield with the source wavefield that is prescribed by the shot-profile migration imaging condition. This basic idea is expanded in the next theoretical section.

THEORY

I first review the basic principles of downward continuation, shot-profile migration, and source-receiver migration. Then I will show the equivalence of shot-profile migration with source-receiver migration.

Downward continuation

Downward continuation is the process of extrapolating the acoustic wavefield along the depth direction. The downward-continuation operator is derived from the one-way wave equation (Claerbout, 1985), and I will refer to it as the Single Square Root (SSR) operator.

In a discretized domain, the SSR operator is a non-stationary convolutional operator that depends locally on the interval velocity. The operator that downward-continues up-going waves (recorded data) can be expressed as

$$e_z^{ik_z z} \overset{\mathbf{m}}{*} P_z(\omega,\mathbf{m}) = \sum_{i_x=-N_x}^{N_x} \sum_{i_y=-N_y}^{N_y} a_{[i_x,i_y]}(z,\mathbf{m})\, P_{z-\Delta z}\left(\omega,\mathbf{m}+i_x\Delta\mathbf{x}_\mathbf{m}+i_y\Delta\mathbf{y}_\mathbf{m}\right), \tag{1}$$

where P_z and $P_{z-\Delta z}$ are the wavefields at depth z and $z-\Delta z$, ω is the temporal frequency, $\mathbf{m}=(x_m,y_m)$ is a horizontal vector in model space, and $\Delta\mathbf{x}_\mathbf{m}$ and $\Delta\mathbf{y}_\mathbf{m}$ are the unit vectors along the horizontal coordinates. The right-hand side of equation (1) represents a two-dimensional convolution of the wavefield $P_{z-\Delta z}$ with the filter coefficients $a_{[i_x,i_y]}(z,\mathbf{m})$. The half-widths of the convolutional operator are N_x and N_y.

In the notation that I introduce for the downward-continuation operator ($e_z^{ik_z z} \overset{\mathbf{m}}{*}$), the symbols

$\overset{\mathbf{m}}{*}$ indicate the convolution over the horizontal axes (x_m, y_m), and the z at the bottom indicates the dependency of the operator from the depth level. Notice that in an arbitrary medium, where velocity varies both vertically and laterally, the operator $e_z^{ik_z z}\overset{\mathbf{m}}{*}$, and thus also the convolutional coefficients $a_{[i_x,i_y]}$, are functions of both depth and the horizontal location. This dependency from the horizontal location is not explicitly manifest from my notation for $(e_z^{ik_z z}\overset{\mathbf{m}}{*})$.

To simplify the discussion I assume that the downward-continuation operator zeroes the evanescent components of the wavefield. Under this assumption, the operator that downward continues the down-going waves (source function) is simply the complex conjugate of the operator expressed in equation (1), and I will represent it as $e_z^{-ik_z z}\overset{\mathbf{m}}{*}$.

Shot-profile migration

In shot-profile migration each record is migrated independently. The receiver wavefield P^g is downward continued starting from the recorded data. The source wavefield $P^s$is downward continued starting from an assumed source wavelet. In this case, I assume that the source is a delta function in the space domain and a constant as a function of frequency (impulse at time zero).

Each wavefield is propagated independently by applying the SSR operator. At each depth level that is,

$$ {}^{\delta}P_z^s(\omega,\mathbf{m};\bar{\mathbf{s}}) = e_{0\to z}^{-ik_z z}\overset{\mathbf{m}}{*}\,\delta(\mathbf{m}-\bar{\mathbf{s}}), \tag{2}$$

and

$$ P_z^g(\omega,\mathbf{m};\bar{\mathbf{s}}) = e_{0\to z}^{ik_z z}\overset{\mathbf{m}}{*}\,P_{z=0}^g(\omega,\mathbf{m};\bar{\mathbf{s}}), \tag{3}$$

where $\bar{\mathbf{s}}$ is the location of the shot. The prefix δ in ${}^{\delta}P_z^s$ indicates that the source function is an impulse. The notation $e_{0\to z}^{ik_z z}$ indicates the convolutional operator resulting from the chain of convolutions that starts at the surface ($z=0$) and ends at depth z. Notice the negative sign in front of the exponential in

equation (2). As discussed above, the negative sign is there because the source wavefield propagates downward, rather than propagating upward as the receiver wavefield does.

The image cube is formed by cross-correlating in time the two wavefields shifted with respect to each other along the horizontal directions. In the frequency domain the cross-correlation is performed by multiplication with the complex conjugate, and it is evaluated at zero lag by summation over frequencies. The horizontal shift is the half offset $\mathbf{h} = (x_h, y_h)$. Notice that the half-offset $\mathbf{h}$ is measured at depth, and thus it has a different role than the more commonly used data offset. To distinguish $\mathbf{h}$ from the data offset, I will refer to it as the *subsurface offset*. The image cube corresponding to the shot at $\bar{\mathbf{s}}$ is thus computed as:

$$I_{\text{shot}}(z, \mathbf{m}, \mathbf{h}) = \Re \left[\sum_{\omega} P_z^g(\omega, \mathbf{m}+\mathbf{h}; \bar{\mathbf{s}}) \overline{P_z^s(\omega, \mathbf{m}-\mathbf{h}; \bar{\mathbf{s}})}^{\delta} \right], \tag{4}$$

where the symbol $\Re$ indicates that the image is the real part of the cross-correlation, and the bar above the wavefield indicates complex conjugation. The image cube for the whole survey is obtained by summing the image cubes for all the shots.

Source-receiver migration

Source-receiver migration is based on the concept of survey sinking. The whole prestack data set is downward-continued at each depth level. After each depth-propagation step, the propagated wavefield is equivalent to the data that would have been recorded if all sources and receivers were placed at the new depth level. This task is accomplished by downward continuing all the source gathers and all the receiver gathers at each depth step. Therefore, the basic downward continuation is performed by a double application of the SSR operator, and it is often referred as the Double Square Root (DSR) operator. At each depth step the wavefield at depth z is computed from the wavefield at depth $z - \Delta z$

as

$$P_z(\omega,\mathbf{g},\mathbf{s}) = e_z^{ik_z z} \overset{\mathbf{g}}{*} e_z^{ik_z z} \overset{\mathbf{s}}{*} P_{z-\Delta z}(\omega,\mathbf{g},\mathbf{s}), \tag{5}$$

where the first (starting from the right) convolution over the source axes $\left(\text{indicated by the symbols } \overset{\mathbf{s}}{*}\right)$ downward-continues the receiver gathers, and the second convolution downward-continues the source gathers.

Because of the commutative properties of the SSR operator that I demonstrate in Appendix A, the wavefield at depth P_z can be expressed as a function of the wavefield at the surface $P_{z=0}$ as

$$P_z(\omega,\mathbf{g},\mathbf{s}) = e_{0\to z}^{ik_z z} \overset{\mathbf{g}}{*} e_{0\to z}^{ik_z z} \overset{\mathbf{s}}{*} P_{z=0}(\omega,\mathbf{g},\mathbf{s}), \tag{6}$$

even if the sinking of the survey is performed recursively, one depth step at a time, using equation (5).

At each depth level, the image is extracted from the downward-continued wavefield by evaluating the wavefield at zero time. The image-space coordinates $(\mathbf{m},\mathbf{h})$ and the source-receiver coordinates $(\mathbf{s},\mathbf{g})$ are linked by the well-known transformations

$$\mathbf{s} = \mathbf{m} - \mathbf{h} \qquad \mathbf{g} = \mathbf{m} + \mathbf{h}. \tag{7}$$

The image cube is then computed by summing all the frequencies and mapping the wavefield into image coordinates by using equation (7); that is,

$$I_{\text{s}-\text{g}}(z,\mathbf{m},\mathbf{h}) = \Re\left[\sum_{\omega} P_z(\omega,\mathbf{m}+\mathbf{h},\mathbf{m}-\mathbf{h})\right]. \tag{8}$$

Equivalence of source-receiver migration and shot-profile migration

For the sake of simplicity, I demonstrate the equivalence of the two migration methods by showing that the images obtained by migrating the traces recorded in a single shot profile are the same. The linearity of both migrations with respect to the input wavefield makes the extension to the full data set obvious.

To create the whole prestack wavefield from the traces recorded in a single shot profile, we add the live traces to a cube of zero traces. The resulting data cube is equal to the outer product of two functions: the first represents the recorded data $P^g_{z=0}(\omega, \mathbf{g}; \bar{\mathbf{s}})$ and is independent of the source-coordinate $\mathbf{s}$. The second function is a delta function that is centered at $\bar{\mathbf{s}}$ and it is independent of the receiver-coordinate $\mathbf{g}$.

From equation (6), the wavefield at depth obtained by survey sinking can thus be expressed as

$$
\begin{aligned}
& P_z(z, \mathbf{g}, \mathbf{s}) \\
&= e^{ik_z z}_{0\to z} \overset{\mathbf{g}}{*} e^{ik_z z}_{0\to z} \overset{\mathbf{s}}{*} \left[P^g_{z=0}(\omega, \mathbf{g}; \bar{\mathbf{s}})\, \delta(\mathbf{s} - \bar{\mathbf{s}}) \right] && (9) \\
&= \left[e^{ik_z z}_{0\to z} \overset{\mathbf{g}}{*} P^g_{z=0}(\omega, \mathbf{g}; \bar{\mathbf{s}}) \right] \left[e^{ik_z z}_{0\to z} \overset{\mathbf{s}}{*} \delta(\mathbf{s} - \bar{\mathbf{s}}) \right] && (10) \\
&= \left[P^g_z(\omega, \mathbf{g}; \bar{\mathbf{s}}) \right] \left[\overline{{}^{\delta} P^s_z(\omega, \mathbf{s}; \bar{\mathbf{s}})} \right]. && (11)
\end{aligned}
$$

The equivalence of expression (9) and expression (11) is crucial to the results presented in this short note; therefore it deserves careful explanations. The step from expression (9) to expression (10) is valid because the recorded data $P^g_{z=0}(\omega, \mathbf{g}; \bar{\mathbf{s}})$ is independent of the source location, and thus it can be pulled out of the convolution along the source axes $\left(\text{i.e. the application of the operator} e^{ik_z z}_{0\to z} \overset{\mathbf{s}}{*}\right)$. The step from expression (10) to expression (11) is justified by comparing the term in the first square bracket with the expression in equation (3), and the the term in the second square bracket with the expression in equation (2). Notice the importance of the negative sign in front of the exponential in equation (2) for deriving the result in equation (11).

Imaging is performed by evaluating the downward-continued wavefield at the appropriate locations, as described by equation (8). If we apply this imaging condition to the wavefield in (11), we

obtain

$$I_{\text{s-g}}(z,\mathbf{m},\mathbf{h}) = \Re\left\{\sum_{\omega}\left[P_z^g(\omega,\mathbf{m}+\mathbf{h};\bar{\mathbf{s}})\right]\left[\overline{{}^{\delta}P_z^s(\omega,\mathbf{m}-\mathbf{h};\bar{\mathbf{s}})}\right]\right\}, \tag{12}$$

which is exactly the same image cube as the image cube obtained by shot-profile migration [equation (4)].

TESTS ON SYNTHETIC DATA SET

To test the theoretical result reached in the previous section, I migrated one shot record from a synthetic data set that was modeled over a medium with strong lateral velocity variations. These velocity variations cause coherent artifacts ("ghost reflectors") in the image produced by migrating a single shot. The test strongly support the theoretical result that in the source-receiver migration the downward continuations along the shot axis and along the receiver axis do indeed commute in the presence of strong lateral variations. It also confirms that the migration artifacts produced by source-receiver migration and shot-profile migration are the same. The data set was kindly provided by Bill Symes of Rice University, and it has been used to study the artifacts produced by different kinds of migrations (Stolk and Symes, 2002). Figure 1 shows the velocity function assumed to model this synthetic data set. The reflector has a simple flat geometry, but a strong velocity anomaly above it creates severe multipathing that challenges different migration schemes. Figure 2 shows the shot profile used for the test; the source location is at -0.5 kilometers. Notice the complex multipathing in the recorded wavefield.

Both the shot-profile migration program and the source-receiver migration program used for the test perform downward continuation by an extended split-step algorithm (Stoffa et al., 1990; Kessinger, 1992) that employs a Lloyd algorithm (Lloyd, 1982) to select the reference velocities (Clapp, 2002). Depending on the variability of the velocity function at each depth level, the algo-

rithm was allowed to select up to ten reference velocities. The source-receiver migration operated on the data sorted in midpoint-offset coordinates, and thus the boundary conditions are different for the two algorithms. This difference is expected to cause small differences in migration artifacts between the two methods.

Figure 3 shows the zero subsurface offset images (equivalent to the stacked images produced by Kirchhoff migration) produced by the two migration methods. The panel on the left shows the image produced by shot-profile migration, and the panel on the right shows the image produced by source-receiver migration. The two images are almost identical, except for small differences in artifacts. Not only is the flat reflector the same in the two images, but so are the strong ghost reflectors that are visible between the surface locations of 0 and 1 kilometers, which are caused by the triplication of the wavepath. To analyze in more details the differences between the two images shown in Figure 3, I show their differences using two different plotting parameters in Figure 4. The two panels show the same section, but displayed with two different values of the clip parameter (the clip parameter controls the dynamic range of the display by "clipping" the displayed amplitudes): in panel a) the image is clipped as for the images shown in Figure 3 and thus it correctly represents the amplitudes of the differences relative to the migrated images (Figure 3); in panel b) the image is clipped independently (4% of the clip used for panel a). Notice that there is no visible energy in in Figure 4a and that only artifacts are present in Figure 4b. None of the coherent events visible in Figure 3 (the true reflector and the ghost reflectors) are present in Figure 4b. The fact that the maximum amplitude of the differences between the images is only a small fraction of the maximum amplitude of the images, together with the observation that none of the coherent events (true and ghost reflections) is present in the difference panel, strongly supports the conclusion that the differences between the images are caused by the different boundary conditions of the downward-continuation methods.

Figure 5 shows the subsurface offset-domain common-image gathers at the surface location of

0.1 kilometers: panel a) shows the shot-profile migration, panel b) the source-receiver migration. Again the images are identical for both the "true" reflector and the ghost reflectors. Figure 6 shows the angle-domain common-image gathers obtained from the offset-domain gathers shown in Figure 5, after a slant stack transformation (Sava et al., 2001). Notice that the "true" reflector gets imaged at both positive and negative aperture angle because of the wavepath triplications. The "ghost" reflectors get imaged in the aperture-angle gap between the two branches of the true reflector.

Figure 7 demonstrates that the artifacts caused by the wavefield triplications disappear when the whole data set (400 shots) is imaged. It shows the results obtained by source-receiver migration when all the shot records are included in the data; it shows the zero subsurface offset image (panel a), the offset-domain common-image gather at the surface location of 0.1 kilometers (panel b), and the angle-domain common-image gather at the surface location of 0.1 kilometers (panel c). Compare the high-quality of these images with the artifact-ridden images shown in with Figures 3, 5 and 6.

CONCLUSIONS

I have theoretically proven that source-receiver migration is exactly equivalent to downward-continuation shot-profile migration. The results of my migration tests confirm the theoretical result. This equivalence is not only valid for the (stacked) migrated image, but also for the velocity and AVA information provided by prestack migration. I therefore believe that this theoretical equivalence ought to be taken into account when analyzing the properties of different wavefield-continuation migration methods with respect to data sampling, migration velocity analysis, and migration amplitudes.

The results presented in this short note are not only important from the theoretical point of view but they have a direct application to 3-D imaging projects. Since the results produced by source-receiver and shot-profile migration are theoretically the same, the choice between the two methods

might depend only on practical considerations, such as relative efficiency and flexibility.

ACKNOWLEDGMENTS

I would like to thank Bill Symes of Rice University for kindly providing the synthetic data set that was used for the tests shown in the paper. I also would like to thank Bob Clapp, Paul Sava and Brad Artman at SEP for developing the programs that I used for the tests. I would like to acknowledge the financial support by the sponsors of the Stanford Exploration Project.

APPENDIX A

COMMUTATIVE PROPERTIES OF DOWNWARD-CONTINUATION OPERATORS

The demonstration of the equivalence of the two migration methods depends on the validity of expression (6). This Appendix demonstrates the validity of expression (6) by proving the following commutative property of the downward-continuation operators,

$$\begin{aligned}
\left(e_0^{ik_z z} \overset{\mathbf{g}}{*} e_0^{ik_z z} \overset{\mathbf{s}}{*}\right) \ldots \left(e_{z-\Delta z}^{ik_z z} \overset{\mathbf{g}}{*} e_{z-\Delta z}^{ik_z z} \overset{\mathbf{s}}{*}\right) \left(e_z^{ik_z z} \overset{\mathbf{g}}{*} e_z^{ik_z z} \overset{\mathbf{s}}{*}\right) &= \\
\left(e_0^{ik_z z} \overset{\mathbf{g}}{*} \ldots e_{z-\Delta z}^{ik_z z} \overset{\mathbf{g}}{*} e_z^{ik_z z} \overset{\mathbf{g}}{*}\right) \left(e_0^{ik_z z} \overset{\mathbf{s}}{*} \ldots e_{z-\Delta z}^{ik_z z} \overset{\mathbf{s}}{*} e_z^{ik_z z} \overset{\mathbf{s}}{*}\right) &= \\
e_{0\to z}^{ik_z z} \overset{\mathbf{g}}{*} e_{0\to z}^{ik_z z} \overset{\mathbf{s}}{*}. & \qquad \text{(A-1)}
\end{aligned}$$

The validity of equality (A-1) can be easily verified if the SSR operator applied along the source axis commutes with the SSR operator applied along the receiver axis at a different depth level.

This property of the SSR operator is obvious for vertically layered media, where downward continuation can be performed in the wavenumber domain. However, it is also valid in presence of lateral velocity variations, because the wavefield is downward-continued along each direction by a

convolution that is independent from the other direction. For example, the sources are downward continued by convolving each receiver gather with a convolutional operator that is non-stationary along the source axis, but is independent of the location of the receiver gather.

The SSR operator applied along the receiver axis of a full prestack wavefield at depth z_1 can be expressed as

$$e^{ik_z z}_{z_1} \overset{\mathbf{g}}{*} P(\omega, \mathbf{g}, \mathbf{s}) = \sum_{i_x=-N_x}^{N_x} \sum_{i_y=-N_y}^{N_y} a_{[i_x,i_y]}(z_1, \mathbf{g})\, P\left(\omega, \mathbf{g} + i_x \Delta \mathbf{x}_\mathbf{g} + i_y \Delta \mathbf{y}_\mathbf{g}, \mathbf{s}\right), \tag{A-2}$$

and the SSR operator applied along the source axis of a full prestack wavefield at depth z_2 can be expressed as

$$e^{ik_z z}_{z_2} \overset{\mathbf{s}}{*} P(\omega, \mathbf{g}, \mathbf{s}) = \sum_{j_x=-N_x}^{N_x} \sum_{j_y=-N_y}^{N_y} b_{[j_x,j_y]}(z_2, \mathbf{s})\, P\left(\omega, \mathbf{g}, \mathbf{s} + j_x \Delta \mathbf{x}_\mathbf{s} + j_y \Delta \mathbf{y}_\mathbf{s}\right). \tag{A-3}$$

Because the convolutional coefficients a are independent of $\mathbf{s}$, and the convolutional coefficients b are independent of $\mathbf{g}$, the following equality holds:

$$\begin{aligned}
&e^{ik_z z}_{z_1} \overset{\mathbf{g}}{*} e^{ik_z z}_{z_2} \overset{\mathbf{s}}{*} P(\omega, \mathbf{g}, \mathbf{s}) = \\
&\quad \sum_{i_x=-N_x}^{N_x} \sum_{i_y=-N_y}^{N_y} a_{[i_x,i_y]}(z_1, \mathbf{g}) \sum_{j_x=-N_x}^{N_x} \sum_{j_y=-N_y}^{N_y} b_{[j_x,j_y]}(z_2, \mathbf{s}) \\
&\qquad P\left(\omega, \mathbf{g} + i_x \Delta \mathbf{x}_\mathbf{g} + i_y \Delta \mathbf{y}_\mathbf{g}, \mathbf{s} + j_x \Delta \mathbf{x}_\mathbf{s} + j_y \Delta \mathbf{y}_\mathbf{s}\right) = \\
&\quad \sum_{j_x=-N_x}^{N_x} \sum_{j_y=-N_y}^{N_y} b_{[j_x,j_y]}(z_2, \mathbf{s}) \sum_{i_x=-N_x}^{N_x} \sum_{i_y=-N_y}^{N_y} a_{[i_x,i_y]}(z_1, \mathbf{g}) \\
&\qquad P\left(\omega, \mathbf{g} + i_x \Delta \mathbf{x}_\mathbf{g} + i_y \Delta \mathbf{y}_\mathbf{g}, \mathbf{s} + j_x \Delta \mathbf{x}_\mathbf{s} + j_y \Delta \mathbf{y}_\mathbf{s}\right) = \\
&e^{ik_z z}_{z_2} \overset{\mathbf{s}}{*} e^{ik_z z}_{z_1} \overset{\mathbf{g}}{*} P(\omega, \mathbf{g}, \mathbf{s}).
\end{aligned} \tag{A-4}$$

This result proves the validity of equality (A-1).

The result in equation (A-4) is not trivial. For example, the SSR operators along the same direction (e.g. $\mathbf{g}$) but at different depth levels (e.g. z_1 and z_2) do not commute, as demonstrated by the following expression:

$$e^{ik_z z}_{z_1} \overset{\mathbf{g}}{*} e^{ik_z z}_{z_2} \overset{\mathbf{g}}{*} P(\omega, \mathbf{g}, \mathbf{s}) =$$

$$\sum_{i_x=-N_x}^{N_x}\sum_{i_y=-N_y}^{N_y} a_{[i_x,i_y]}(z_1,\mathbf{g}) \sum_{j_x=-N_x}^{N_x}\sum_{j_y=-N_y}^{N_y} a_{[j_x,j_y]}\left(z_2,\mathbf{g}+i_x\Delta\mathbf{x_g}+i_y\Delta\mathbf{y_g}\right)$$
$$P\left[\omega,\mathbf{g}+(i_x+j_x)\Delta\mathbf{x_g}+\left(i_y+j_y\right)\Delta\mathbf{y_g},\right]\neq$$
$$\sum_{j_x=-N_x}^{N_x}\sum_{j_y=-N_y}^{N_y} a_{[j_x,j_y]}(z_2,\mathbf{g}) \sum_{i_x=-N_x}^{N_x}\sum_{i_y=-N_y}^{N_y} a_{[i_x,i_y]}\left(z_1,\mathbf{g}+j_x\Delta\mathbf{x_g}+j_y\Delta\mathbf{y_g}\mathbf{g}\right)$$
$$P\left[\omega,\mathbf{g}+(i_x+j_x)\Delta\mathbf{x_g}+\left(i_y+j_y\right)\Delta\mathbf{y_g},\right]=$$

$$e^{ik_z z}_{z_2} \overset{\mathbf{g}}{*} e^{ik_z z}_{z_1} \overset{\mathbf{g}}{*} P(\omega,\mathbf{g},\mathbf{s}). \tag{A-5}$$

REFERENCES

Berkhout, A. J., 1984, Seismic migration: imaging of acoustic energy by wave field extrapolation (B. Practical Aspects): Elsevier.

Biondi, B., and Palacharla, G., 1996, 3-D prestack migration of common-azimuth data: Geophysics, **61**, 1822–1832.

Biondi, B., and Sava, P., 1999, Wave-equation migration velocity analysis: 69th Ann. Internat. Meeting, Soc. of Expl. Geophys., Expanded Abstracts, 1723–1726.

Biondi, B., and Shan, G., 2002, Prestack imaging of overturned reflections by reverse time migration: 72nd Ann. Internat. Meeting, Soc. of Expl. Geophys., Expanded Abstracts, 1284–1287.

Claerbout, J. F., 1985, Imaging the Earth's Interior: Blackwell Scientific Publications.

Clapp, R., and Biondi, B., 2000, Tau domain migration velocity analysis using angle CRP gathers and geologic constrains: 70th Ann. Internat. Mtg., Soc. Expl. Geophys., Expanded Abstracts, 926–929.

Clapp, R. G., 2002, Reference velocity selection by a generalized Lloyd method: SEP–**111**, 215–225.

de Bruin, C. G. M., Wapenaar, C. P. A., and Berkhout, A. J., 1990, Angle-dependent reflectivity by means of prestack migration: Geophysics, **55**, no. 9, 1223–1234.

Jacobs, B., 1982, The prestack migration of profiles: Ph.D. thesis, Stanford University.

Jeannot, J. P., 1988, Full prestack versus shot record migration: Practical aspects: 58th Ann. Internat. Meeting, Soc. of Expl. Geophys., Expanded Abstracts, Session:S12.2.

Kessinger, W., 1992, Extended split-step Fourier migration: 62nd Ann. Internat. Meeting, Soc. of Expl. Geophys., Expanded Abstracts, 917–920.

Lloyd, S. P., 1982, Least squares quantization in pcm: IEEE Transactions on Information Theory, **42**, no. 28, 127–135.

Prucha, M., Biondi, B., and Symes, W., 1999, Angle-domain common-image gathers by wave-equation migration: 69th Ann. Internat. Meeting, Soc. Expl. Geophys., Expanded Abstracts, 824–827.

Rickett, J., and Sava, P., 2002, Offset and angle-domain common image-point gathers for shot-profile migration: Geophysics, **67**, 883–889.

Sava, P., Biondi, B., and Fomel, S., 2001, Amplitude-preserved common image gathers by wave-equation migration: 71st Ann. Internat. Meeting, Soc. Expl. Geophys., Expanded Abstracts, 296–299.

Stoffa, P. L., Fokkema, J., de Luna Freire, R. M., and Kessinger, W. P., 1990, Split-step Fourier migration: Geophysics, **55**, no. 4, 410–421.

Stolk, C., and Symes, W., 2002, Artifacts in Kirchhoff common image gathers: 72nd Ann. Internat. Meeting, Soc. of Expl. Geophys., Expanded Abstracts, 1129–1132.

Wapenaar, C. P. A., and Berkhout, A. J., 1987, Full prestack versus shot record migration: 69th Ann. Internat. Meeting, Soc. of Expl. Geophys., Expanded Abstracts, Session:S15.7.

Wapenaar, K., Van Wijngaarden, A., van Geloven, W., and van der Leij, T., 1999, Apparent AVA effects of fine layering: Geophysics, **64**, no. 6, 1939–1948.

LIST OF FIGURES

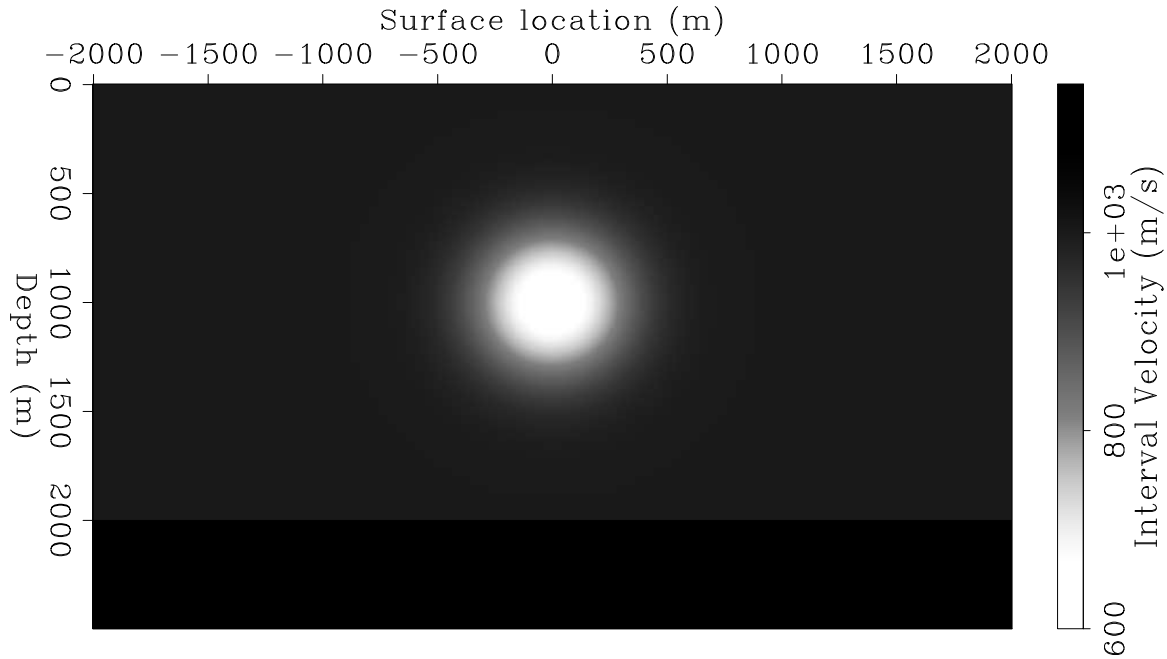
Surface location (m)
−2000 −1500 −1000 −500 0 500 1000 1500 2000
Depth (m)
0 500 1000 1500 2000
Interval Velocity (m/s)
600 800 1e+03

Figure 1.

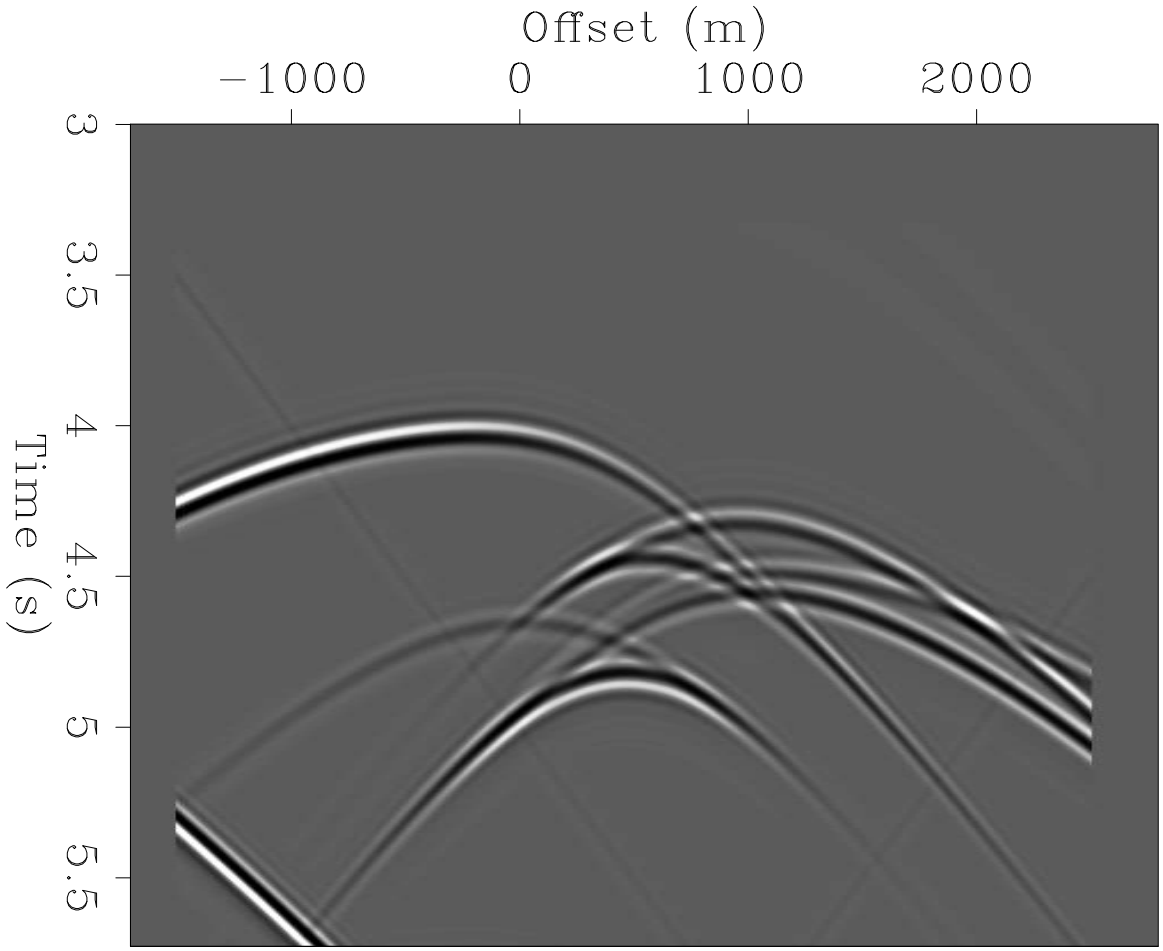

Figure 2.

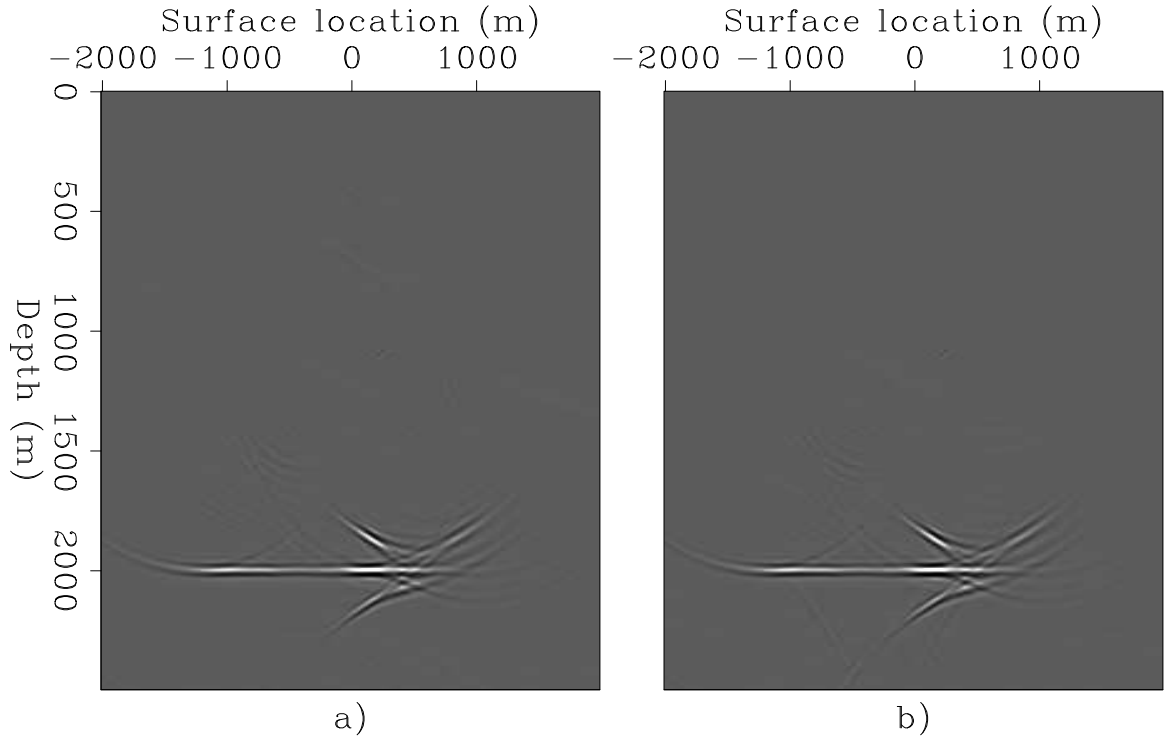
Surface location (m)
−2000 −1000 0 1000
Surface location (m)
−2000 −1000 0 1000
0
500
1000
1500
2000
Depth (m)
a)
b)

Figure 3.

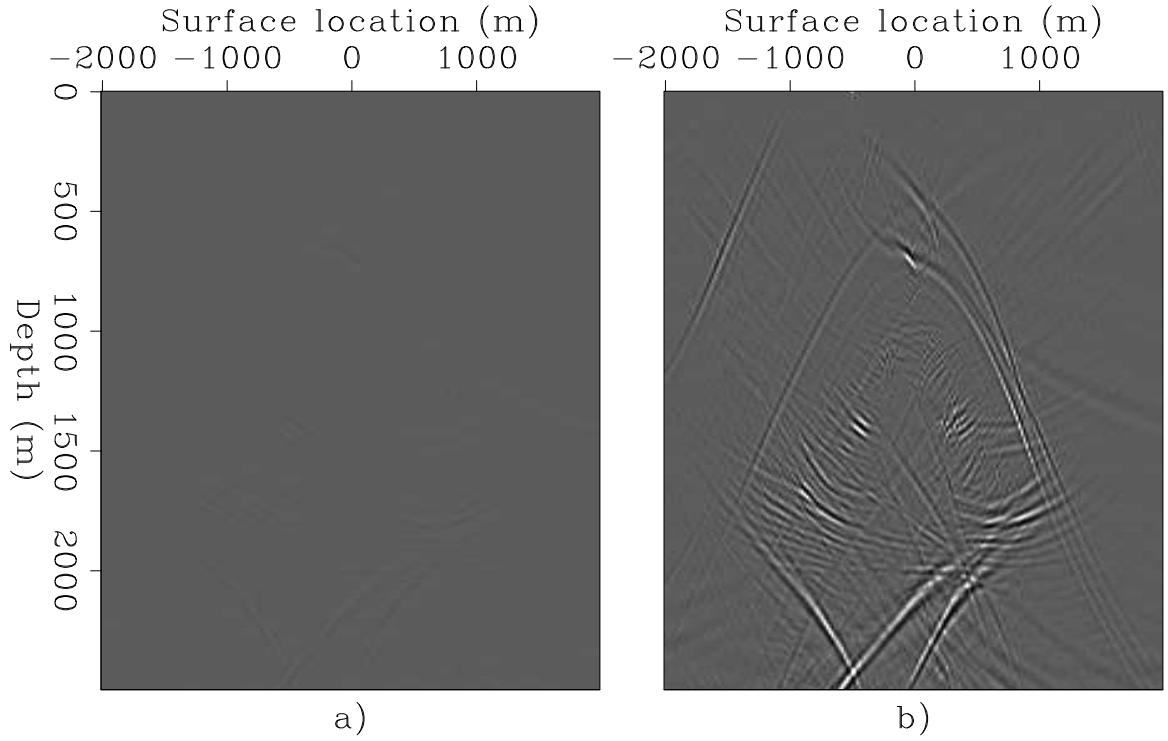
Surface location (m)
−2000 −1000 0 1000
Surface location (m)
−2000 −1000 0 1000
0
500
1000
1500
2000
Depth (m)
a)
b)

Figure 4.

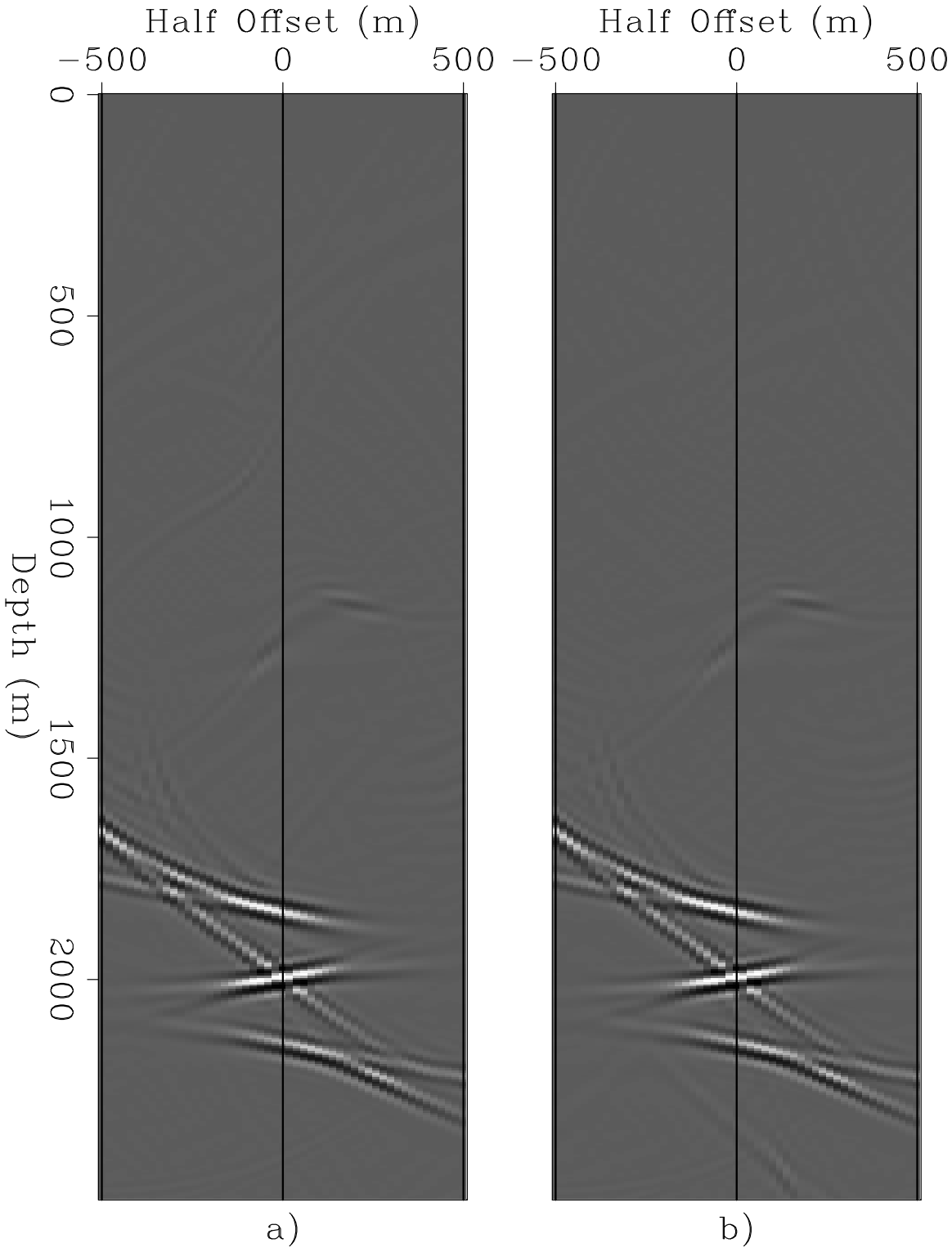
Half Offset (m)
−500
0
500
Half Offset (m)
−500
0
500
0
500
1000
1500
2000
Depth (m)
a)
b)

Figure 5.

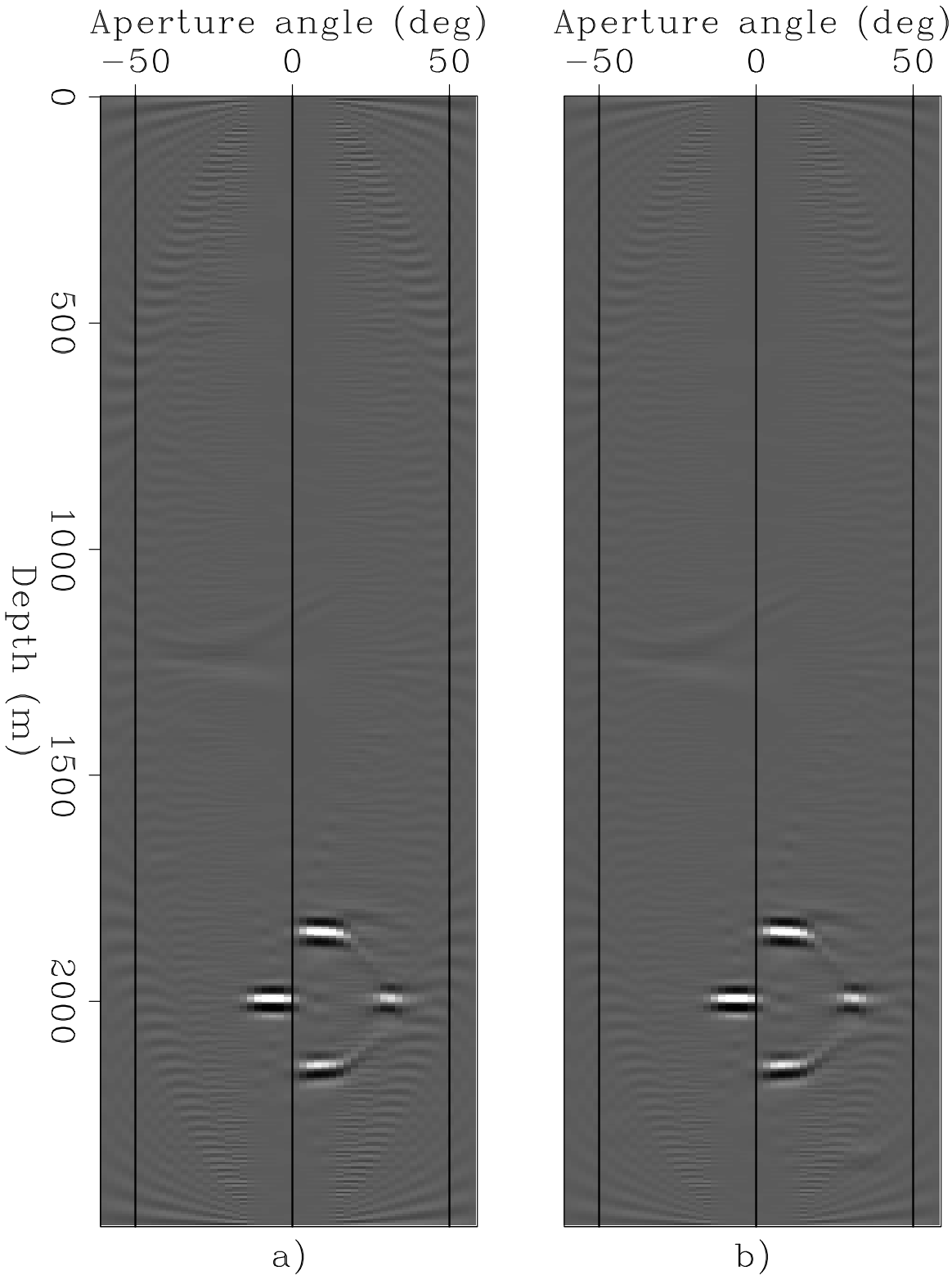
Aperture angle (deg)
−50
0
50
Aperture angle (deg)
−50
0
50
0
500
1000
1500
2000
Depth (m)
a)
b)

Figure 6.

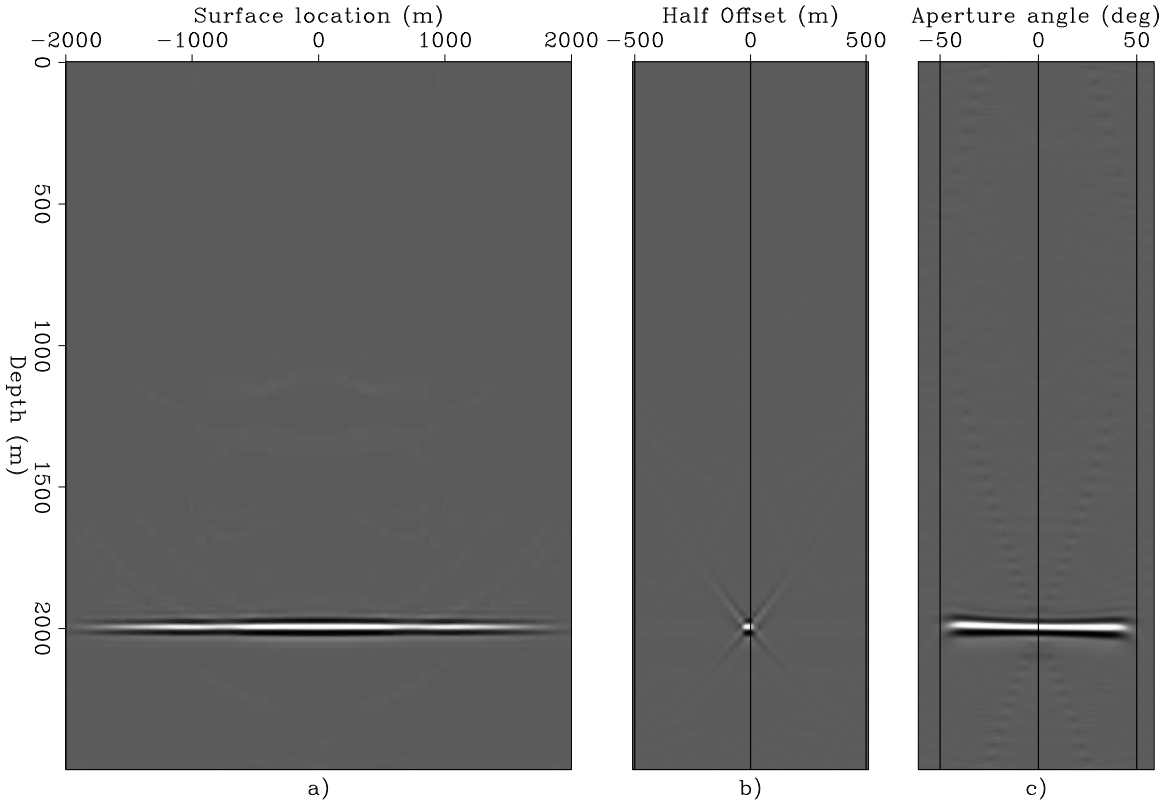
Surface location (m)
−2000
−1000
0
1000
2000
Half Offset (m)
−500
0
500
Aperture angle (deg)
−50
0
50
Depth (m)
0
500
1000
1500
2000
a)
b)
c)

Figure 7.